Guidance and Control Co-Design for Enhanced Performance of Fixed-Wing UAVs

Sabine Wisbacher * **Roser Berenguer Bertran** ** **Martin Guist** **
Daniel Ossmann * **Harald Pfifer** **

* *Munich University of Applied Sciences HM, 80335 Munich, Germany (e-mail: {sabine.wisbacher, daniel.ossmann}@hm.edu)*
** *Chair of Flight Mechanics & Control, TU Dresden, 01069 Dresden, Germany (e-mail: {roser.berenguer_bertran, martin.guist, harald.pfifer}@tu-dresden.de)*

Abstract: This paper presents the design and flight test validation of a co-designed guidance and control system for a fixed-wing unmanned aerial vehicle (UAV). The co-design of all integrated control loops enables increased performance capabilities which are especially important for highly dynamic UAV missions. The control design is based on a mixed-sensitivity control approach to enable robust inner loop controls in the presence of uncertainties. The guidance design implements a look-ahead path following algorithm which enables superior performance metrics while considering the computational constraints present for small UAV systems. The co-designed guidance and control approach is applied to a small fixed-wing UAV and flight tested mimicking a highly dynamic urban flight trajectory. The flight-test results not only validate the seamless implementation of the developed algorithms on the available flight-control computer, but also demonstrate their robust performance during real-world operations.

Keywords: Aerospace Guidance and Control; Robust Control; Flight Test.

1. INTRODUCTION

Unmanned Aerial Vehicles (UAVs) have become important assets across a wide range of civil and military applications due to their versatility and operational flexibility. Fixed-wing UAVs are particularly suited for missions that require long-range flights and larger payload capacities. As these UAVs are deployed in complex environments, new operational challenges emerge. For example, urban flight operations impose stringent safety and performance requirements. Narrow flight corridors between buildings and rapidly changing atmospheric conditions demand precise trajectory tracking and robust control performance. These challenges are especially pronounced for small fixed-wing UAVs, whose relatively low cruise speeds and limited control authority make them more sensitive to external disturbances. Thus reliable guidance and control under such conditions is essential to ensure mission success. Achieving this level of performance requires a close integration between guidance and control system design. Conventional sequential design approaches, where guidance laws and control loops are developed independently, are not able to fully exploit system capabilities. In contrast, guidance and control co-design methodologies explicitly consider these interactions in the design process, enabling joint optimization of both subsystems to improve robustness and trajectory-following performance.

This paper introduces a guidance and control system architecture which allows to efficiently co-design and tune the guidance and control laws together. The control design employs robust control techniques while the guidance incorporates intuitive tuning parameters easily adaptable to the achieved controller performance. In contrast to the well-established approach in Park et al. (2004), which offers a single global tuning variable, the guidance method herein provides additional flexibility for tailoring the guidance behavior to the underlying control performance. The proposed system architecture is developed and flight tested on an urban-like, highly dynamic trajectory for a small fixed-wing UAV. In literature, classical control co-design approaches via the joint optimization of control system together with the aircraft layout are found in Wauters et al. (2023) for mission-specific flight paths, yielding efficiency improvements for highly repetitive tasks. Control co-design has been explored for multi-copters in Mabboux et al. (2024) and Bosio and Mueller (2025), providing improvement in robustness and energy efficiency. An H_∞-based controller in combination with a proportional–integral positioning guidance is developed in Mabboux et al. (2024). A guidance and control system using H_∞-based controllers for lateral attitude tracking and a nonlinear guidance logic is provided in Razar (2008). None of these contributions, however, explicitly target guidance and control co-design. The herein proposed guidance and control algorithm is developed within a unified design framework that begins with the inner most control laws. It provides a systematic and physically grounded design methodology that can be interpreted and tuned intuitively. The controller design is based on H_∞ synthesis and single-input single-output (SISO) loop-shaping to achieve maximum bandwidth while maintaining robust performance. The guidance strategy employs a look-ahead path-following algorithm to generate the information required for the proposed target-point-following structure. Based on the fundamentals of these techniques in Section 2, the proposed guidance and control system architecture in Section 3 enables efficient co-design and analytically grounded fine-tuning. Detailed in Section 4, the co-designed architecture is developed for a small fixed wing UAV. The flight-test campaign, presented in Section 5, indicates satisfactory tracking results for the defined trajectory, confirming the applicability of the presented system architecture.

2. FUNDAMENTALS

The unified design approach presented herein consists of H_∞ and SISO loop-shaped controllers and employs a guidance structure with intuitive tuning parameters as the outer loop. The fundamentals of this design approach, consisting of the weighting scheme used for the synthesis of the proposed H_∞ controllers and the look-ahead path-following algorithm are given below.

2.1 H_∞ Weighting Scheme

Ensuring robust performance is especially important for UAVs as usually the flight dynamic models aren't properly validated via flight-test based system identification. Using H_∞-based control designs can provide inherent robustness towards model uncertainties by choosing meaningful weighting structures, which help shaping the relevant closed loop transfer functions, allowing to push up performance. Closed-loop shaping techniques seek to directly shape different sensitivity channels of the closed-loop controller-plant interconnection through weighted H_∞-norm optimization and are commonly referred to as mixed sensitivity (Skogestad and Postlethwaite, 2005). A suitable weighted closed-loop interconnection scheme is provided in (Theis et al., 2020). The input-output map from the performance inputs w to the performance outputs z is given by

$$\begin{bmatrix} z_1 \\ z_2 \end{bmatrix} = \begin{bmatrix} W_e U_e^{-1} & 0 \\ 0 & W_u U_u^{-1} \end{bmatrix} \begin{bmatrix} -SP & S \\ -KSP & KS \end{bmatrix} \begin{bmatrix} U_d & 0 \\ 0 & U_e \end{bmatrix} \begin{bmatrix} w_1 \\ w_2 \end{bmatrix}, \quad (1)$$

where K denotes the controller to be designed, P the underlying plant, and $S = (I + PK)^{-1}$ the sensitivity. The desired closed-loop properties are enforced via the frequency-dependent weights W_u and W_e. The constant matrices U_e, U_u, and U_d provide appropriate input–output scaling. The H_∞ control design algorithm aims to internally stabilize the interconnection (1) and minimize the H_∞-norm from w to z via the controller K. For the controller synthesis, the generalized plant G, depicted in Fig. 1, is obtained by augmenting the plant P with the weights and scaling matrices. Finally, the convex optimization problem

$$\min_{K} ||\mathscr{F}_L(G,K)||_\infty \quad (2)$$

to find K needs to be solved, where $\mathscr{F}_L(G,K)$ denotes the lower linear fractional transformation between the generalized plant G and the controller. Herein, K is synthesized using MATLAB's Robust Control Toolbox.

2.2 Look-Ahead Path Following

The guidance law is designed to steer the aircraft towards a moving target point along a given trajectory. The moving target point is calculated using a look-ahead path-following algorithm as employed in Sedlmair et al. (2022); Berenguer Bertran et al. (2025). The algorithm determines a target point by computing the intersection points of a three-dimensional sphere around the aircraft position with the trajectory. It requires a continuous analytical representation of the trajectory, which is found by fitting a cubic spline of the form

$$S_k(\tau) = m_{0,k} + m_{1,k}\tau + m_{2,k}\tau^2 + m_{3,k}\tau^3 \quad (3)$$

to the trajectory shape, where $k \in 1,\ldots,n$ denotes the spline segment index and n the total number of segments required to accurately represent the trajectory. Each segment is valid only within a specific range $\tau = [\tau_{\min,k}, \tau_{\max,k}]$. The coefficients $m_{i,k} \in \mathbb{R}^3$ define the cubic polynomial for each segment in north, east and vertical direction. To enable transitions from one segment to the next the functions need to be joint together smoothly. The analytical representation (3) of the trajectory is used to determine the intersection points between the sphere around the aircraft position p_a and the trajectory, given by

$$||S_k(\tau) - p_a|| = R \quad (4)$$

where R is the radius of the sphere, resulting in a sixth-order polynomial depending on these variables. The roots of this polynomial are the intersection points τ_1 and τ_2 as visualized in Fig. 2. In general the point τ_2 is selected as target point. Note that tracking accuracy increases with decreasing search radius due to finer trajectory sampling; however, overly small radii may exceed the UAV's capability.

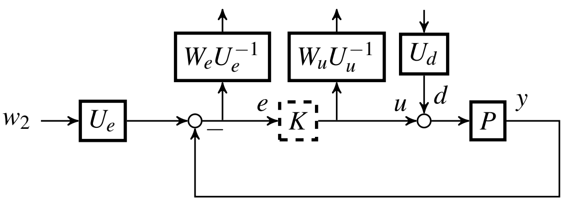

Fig. 1. Generalized plant G for the H_∞-based controller design.

3. SYSTEM ARCHITECTURE

Optimized planning of UAV flight missions via the generation of sophisticated flight trajectories has become an important prerequisite specially in highly dynamic flight scenarios. For instance, in Rienecker et al. (2025) the flight path illustrated in Fig. 3 is optimized for energy efficiency while accounting for local wind phenomena in an urban environment. Following such trajectories tightly requires a highly optimized, co-designed guidance and flight control system.

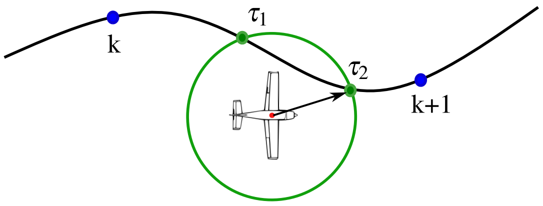

Fig. 2. Target point selection of the look-ahead path following.

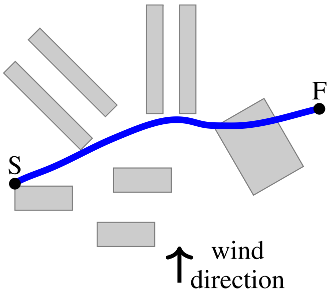

Fig. 3. Energy optimal trajectory (━) from the starting point (S) to the finish (F) passing through and over buildings (▭) in an urban environment.

3.1 Guidance and Control Structure

To enable highly dynamic flight trajectories, a guidance and control structure as depicted in Fig. 4, is proposed. The two control laws incorporate open- and closed-loop shaping control designs enabling fast and accurate tracking while proving a sufficient degree of robustness against uncertainties. In detail, they generate commands for elevator deflection δ_E and thrust δ_T based on flight-path angle and speed references, i.e. γ_{cmd} and V_{cmd}, in the longitudinal axis, and commands for aileron deflection δ_A and rudder deflection δ_R based on bank angle reference φ_{cmd} in the lateral axis.

The aforementioned references are provided to the control loops by the guidance, which employs two main components: Firstly, the target point calculation, which uses a look-ahead algorithm. It employs a search radius around the measured three-dimensional aircraft position $p_a = [x_a, y_a, h_a]$ to constantly calculate the next target point along a given trajectory $\mathscr{T}$ as described in Section 2.2. Since the longitudinal and lateral control laws are decoupled, the guidance is likewise separated into corresponding channels. This enables an optimized guidance and control co-design of each loop with respect to its own dynamic constraint imposed by the control loops.

Based on the longitudinal target point, the algorithm provides a target altitude h_t for the vertical tracking of the trajectory. Based on the lateral target point, a reference heading χ_{ref}, corresponding to the nominal trajectory heading at the computed reference point, and the lateral deviation d_{lat}, defined as the horizontal distance between the aircraft and the target point perpendicular to the segment heading, are computed. Secondly, the target point following employs physically motivated guidance laws to process the information provided by the target point calculation to a flight-path angle command γ_{cmd} for the longitudinal axis and a roll attitude command φ_{cmd} for the lateral axis, which are both forwarded to the control laws. This guidance approach is designed for intuitive and straightforward tuning, facilitating an effective co-design of the overall guidance and attitude control system.

3.2 System Architecture Deployment

The proposed system architecture is developed for the Urban Condor X, a UAV developed at the Chair of Flight Mechanics and Control at TU Dresden. It is based on an Sig Kadet LT-40 airframe, which has been upgraded with a redesigned, 3D-printed wing for higher payloads and an extended operational flight envelope. Depicted in Fig. 5, the aircraft weights 7.5 kg at a wingspan of 2 m and has a cruise speed of 20 m/s. A Pixhawk 6x flight control unit enables manual or autonomous flight via actuating the control surfaces and electric motor through the control algorithms. The Pixhawk 6x also provides the required measurements for the used guidance and control system via its GPS, inertial measurement unit, barometers, and a pitot-static system. The system architecture is deployed on the Pixhawk using the Simulink PX4 toolbox, which enables the direct development of customized software in Matlab. A nonlinear simulation model of the UAV is available for simulation-based verification of the developed algorithms, featuring identified aerodynamic characteristics from wind tunnel and flight tests conducted in Wisbacher et al. (2025) and Franke et al. (2026). Linearization capabilities allow the generation of linear models for model based control design purposes.

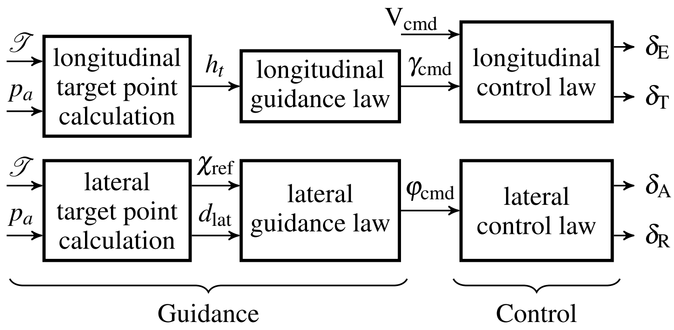

Fig. 4. Proposed guidance and control architecture.

Fig. 5. The UAV test vehicle Urban Condor X.

4. GUIDANCE AND CONTROL CO-DESIGN FOR THE URBAN CONDOR X

This section details the controller and guidance co-design of for the Urban Condor X, starting with the most inner control loops and making its way to the outer guidance strategy.

4.1 Controllers

Figure 6 depicts the architecture of the control system. Due to the low coupling in the two axes, the longitudinal and lateral control loops can be designed separately.

Longitudinal Control Law This flight control law consists of an inner-loop load factor (n_z) tracker and an outer-loop longitudinal flight path (γ) and airspeed (V) tracker. The n_z-tracker is designed using the short period approximation of the aircraft, see, e.g., Theis et al. (2018). The SISO loop is shaped via open-loop shaping (Skogestad and Postlethwaite, 2005), resulting in the controller transfer function

$$k_{n_z}(s) = \tilde{k}\frac{s+\omega_I}{s} \cdot \frac{bs+\omega_L}{s+b\omega_L} \cdot \frac{\omega_{ro}}{s+\omega_{ro}}. \tag{5}$$

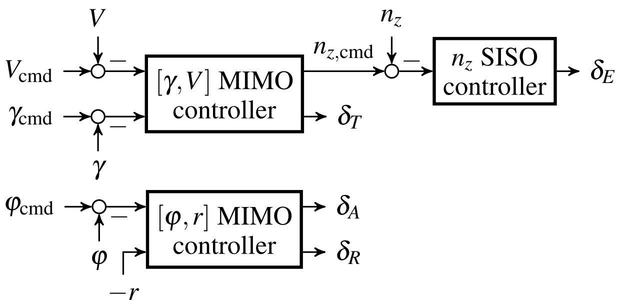

Fig. 6. Detailed longitudinal and lateral control laws.

In (5), the integrator with its lead part at $\omega_I = 5\,\mathrm{rad/s}$ is added to enable tracking of the load factor below 5 rad/s. The roll-off at $\omega_{ro} = 15\,\mathrm{rad/s}$ reduces the magnitude of frequencies above 15 rad/s to be well below the actuator bandwidth. The lead filter with $\omega_L = 13\,\mathrm{rad/s}$ and $b = \omega_L/8$ improves the tracking behavior. The gain $\tilde{k} = 9.5$ finally adjusts the open-loop crossover frequency to 5.5 rad/s, which is close to the short-period frequency of the Urban Condor X. The resulting gain margin is 6.95 dB and the phase margin 54.1°, determined on the full order longitudinal model. These values are above the common requirements of 6 dB gain and 45° phase margins.

The outer loop of the longitudinal motion is a multi-input multi-output (MIMO) system, where airspeed and flight-path angle commands, i.e., V_{cmd} and γ_{cmd}, are tracked via thrust and load factor. Due to the coupling in the MIMO system, closed-loop mixed sensitivity H_∞ shaping is employed. The weightings

$$W_e(s) = \begin{bmatrix} \frac{s+\omega_V\sqrt{3}}{2s+\varepsilon\omega_V\sqrt{3}} & 0 \\ 0 & \frac{s+\omega_\gamma\sqrt{3}}{2s+\varepsilon\omega_\gamma\sqrt{3}} \end{bmatrix} \tag{6}$$

and

$$W_u(s) = \begin{bmatrix} \frac{s+\omega_T}{0.01s+\omega_T} & 0 \\ 0 & \frac{s+\omega_{n_z}}{0.01s+\omega_{n_z}} \end{bmatrix} \tag{7}$$

are used for the synthesis (Berenguer Bertran et al., 2025). $W_e(s)$ has integral behavior up to $\omega_V = \omega_\gamma = 2\,\mathrm{rad/s}$ and a magnitude of 0.5 beyond. The parameter $\varepsilon = 0.01$ constraints the tracking error in both channels to 1 %. $W_u(s)$ has unit gain up to a roll-off frequency of $\omega_T = 10\,\mathrm{rad/s}$ for the thrust and of $\omega_{n_z} = 5\,\mathrm{rad/s}$ for the load factor. While $W_e(s)$ effectively demands an integral behavior at low frequencies in both channels to enable airspeed and flight-path angle tracking, the low pass behavior of $W_u(s)$ ensures the roll-off of the controller below the available actuation bandwidth. Additionally, constant weights $U_e = \mathrm{diag}(1\,\mathrm{m/s}, 0.5°)$, $U_u = \mathrm{diag}(5\,\mathrm{N}, 0.025)$ and $U_d = \mathrm{diag}(0.5\,\mathrm{N}, 0.005)$ are used for scaling the interconnection.

Using the full-order longitudinal model, single-loop gain- and phase-margins result in 24.2 dB and 68.6° for the airspeed channel and 11.3 dB and 54.5° for the flight-path channel. The plots in Fig. 7 show the sensitivity S on the left and controller sensitivity KS on the right, both indicated via (—), for the flight-path angle channel together with the inverse of their corresponding weights (—), i.e., W_e^{-1} and $W_u^{-1}U_u/U_e$, respectively. Despite sensitivity exceeding the weighting functions at some frequencies, the resulting behavior is satisfactory. In the airspeed channel the results look similar, confirming a successful tracking design via S and an adequate controller roll-off design via KS for all channels.

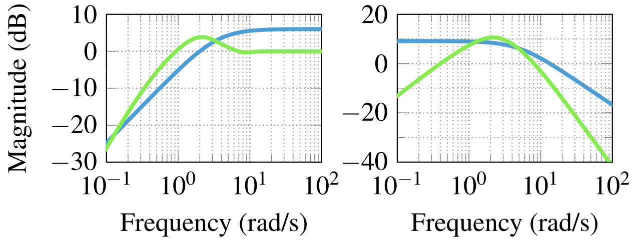

Fig. 7. Flight-path angle channel sensitivity (left) and controller sensitivity (right), both indicated via (—), with respect to the inverse of their weighting functions (—).

Lateral Control Law This law enables bank angle (φ) tracking together with yaw rate (r) feedback for coordinated turns. Again, due to the coupling in the channels, a closed-loop mixed sensitivity H_∞ shaping is employed. The weight

$$W_e(s) = \begin{bmatrix} \frac{s+\omega_\varphi\sqrt{3}}{2s+\varepsilon\omega_\varphi\sqrt{3}} & 0 \\ 0 & 0.5 \end{bmatrix} \tag{8}$$

demands integral behavior up to frequencies of $\omega_\varphi = 6\,\mathrm{rad/s}$ with a tracking error of 1 % ($\varepsilon = 0.01$) in the bank angle channel, while a constant gain of 0.5 for the yaw-rate channel enables yaw damping. The weight

$$W_u(s) = \begin{bmatrix} \frac{s+\omega_A}{0.01s+\omega_A} & 0 \\ 0 & \frac{s+\omega_{R,1}}{s+0.01\omega_{R,1}}\,\frac{s+\omega_{R,2}}{0.01s+\omega_{R,2}} \end{bmatrix} \tag{9}$$

has unit gain up to a desired roll-off frequency of $\omega_A = 20\,\mathrm{rad/s}$ and differentiating behavior beyond in the aileron channel to respect the ailerons bandwidths (Theis et al., 2020) in the design. In the rudder channel the weight has approximately unit gain between $\omega_{R,1} = 0.5\,\mathrm{rad/s}$ and $\omega_{R,2} = 20\,\mathrm{rad/s}$ and it has increasing gain outside that frequency range. Such a weighting is necessary to avoid excitation at high frequencies and to reduce control action in response to wanted turning flights with a nonzero yaw rate. Additionally, constant scaling weights $U_e = \mathrm{diag}(60°, 25°/\mathrm{s})$, $U_u = \mathrm{diag}(25°, 25°)$ and $U_d = \mathrm{diag}(5°, 5°)$ ensure an adequate scaling of the channels for the optimization.

The achieved gain and phase margins are 10.6 dB and 59° for the bank angle channel and 13.1 dB and 71° for the yaw rate channel, confirming high robustness against model uncertainties. Figure 8 shows the inverse of the weight, i.e., $W_e^{-1}(s)$ (—), together with the sensitivity S (—), while Fig. 9 depicts the channels of the controller sensitivity KS (—) with respect to the inverse of the weight, i.e., $W_u^{-1}U_u/U_e$ (—). Again, both figures confirm a successful design process.

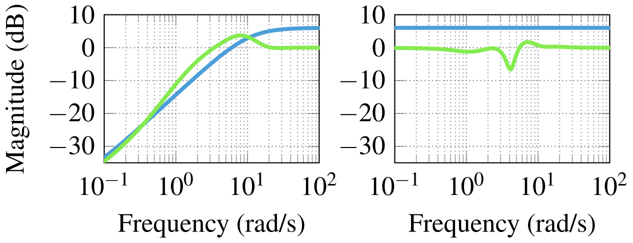

(a) φ-channel (b) r-channel

Fig. 8. Channels of the lateral sensitivity (—) with respect to the inverse of their weighting functions (—).

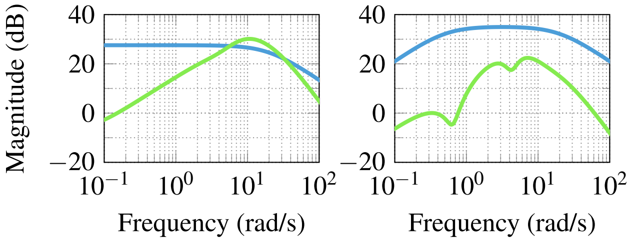

(a) φ-channel (b) r-channel

Fig. 9. Channels of lateral controller sensitivity (—) with respect to the inverse of their weighting functions (—).

4.2 Guidance

Figure 10 depicts the detailed structure of the guidance strategy. As described in Section 3.1, the longitudinal and lateral guidance laws can be designed independently, consistent with the independent design of their respective control laws.

Longitudinal Guidance The target point's altitude h_t provided by the look-ahead algorithm via solving (4) for $R = R_{\text{long}}$ is used directly to calculate the flight-path angle command

$$\gamma_{\text{cmd}} = \sin\left(\frac{h_t - h_a}{R_{\text{long}}}\right) \tag{10}$$

necessary to reach that target point's altitude. Thus, in the altitude guidance law (10) the error between the demanded altitude h_t at the target point and the UAV's current altitude h_a, together with the length of the search radius R_{long}, provides the flight-path command. The search radius is set to $R_{\text{long}} = 30\,\text{m}$, which in a linear analysis yields a bandwidth of 0.66 rad/s. This corresponds to about 33 % of the controller bandwidth, ensuring adequate bandwidth separation of the cascaded loops.

Lateral Guidance Since the lateral dynamics of the UAV are faster than the longitudinal, the lateral search radius is reduced to $R_{\text{lat}} = 15\,\text{m}$ to determine the target points solving (4). As illustrated in Fig. 11, the nominal heading χ_{ref} of the trajectory at the derived target point together with the lateral deviation d_{lat} between the aircraft and this target point is used to compute the required heading command

$$\chi_{\text{cmd}} = \chi_{\text{ref}} + k_\chi \cdot d_{\text{lat}}. \tag{11}$$

In the lateral deviation guidance law (11), the proportional gain is chosen at $k_\chi = 0.02$, which corresponds to a commanded heading change of about one degree per meter of lateral deviation. Note that this strategy of computing the heading command χ_{cmd} together with a large enough setting of k_χ enables the aircraft to align with the trajectory prior to reaching the target point itself, as shown for a sequence of three temporal positions along the captured trajectory in Fig. 11.

Based on the heading command χ_{cmd}, the bank angle command φ_{cmd} for the bank angle controller is generated using a heading guidance law. Within this guidance law, a proportional gain $k_{\dot\Psi}$ converts the heading error $e_\chi = \chi_{\text{cmd}} - \chi$ to the desired turn rate $\dot\Psi$. The conversion from this desired turn rate to the actual bank angle command φ_{cmd} is performed using the ground speed v_{gnd} and gravity g according to the coordinated turning equation, see Schmidt (2012). Finally, the heading guidance law is given by

$$\varphi_{\text{cmd}} = \tan^{-1}\left(\frac{v_{\text{gnd}}}{g}\dot\Psi\right) = \tan^{-1}\left(\frac{v_{\text{gnd}}}{g}k_{\dot\Psi}e_\chi\right). \tag{12}$$

The selection of $k_{\dot\Psi} = 1.8$ for the given application ensures a fast turning of the UAV towards the desired heading without too large bank angle commands. A linear analysis of this heading law results in a bandwidth of 1.79 rad/s, which are ≈ 32 % of the controller bandwidth.

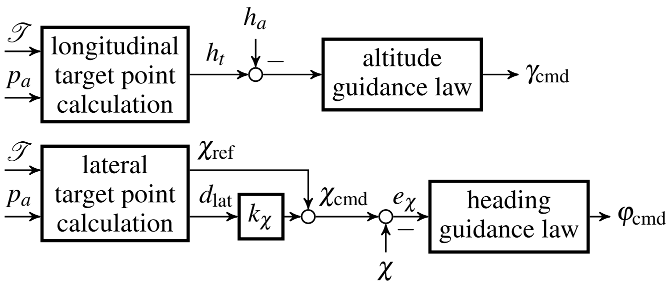

Fig. 10. Detailed structure of the guidance strategy.

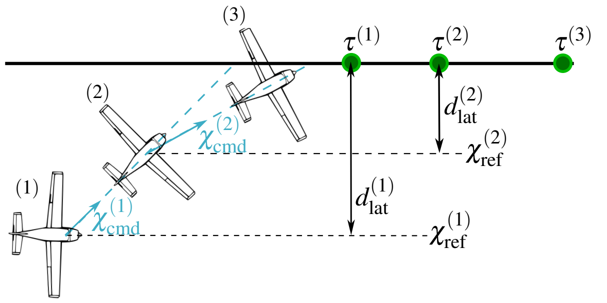

Fig. 11. Illustration of the aircraft capturing the trajectory via the nominal heading χ_{ref} and the lateral deviation d_{lat}.

Overall the presented guidance scheme is easily adaptable in case tuning of itself or the control laws is required. It allows to fully exploit the benefits of advanced control design schemes and supports the exploration of the given system constraints.

5. FLIGHT TEST VALIDATION

The co-designed guidance and control architecture is validated using the Urban Condor X test aircraft in flight on the energy-optimal trajectory presented in Section 3. Although this trajectory is ultimately intended for operation in an urban environment, for test purposes, it is transferred to the model airfield of the TU Dresden (N 50°58'25.68", E 13°44'42.72") that is used as test area. To fit the environment of the airfield, it is also slightly rotated. In the test campaign, the trajectory runs along a constant altitude of 433 m above mean sea level (MSL), which is approximately 100 m above ground-level at the airfield. All flights are conducted at the aircraft's cruising speed of 20 m/s.

In each test flight the UAV is flown manually to different starting positions before enabling the guidance and control system. The guidance then steers the aircraft towards the trajectory and navigates it along the flight path. In total, the trajectory has been flown seven times. The ground tracks of those flights are depicted in Fig. 12 via (- - -), together with the desired flight path (━━). Note that for readability the coordinates are

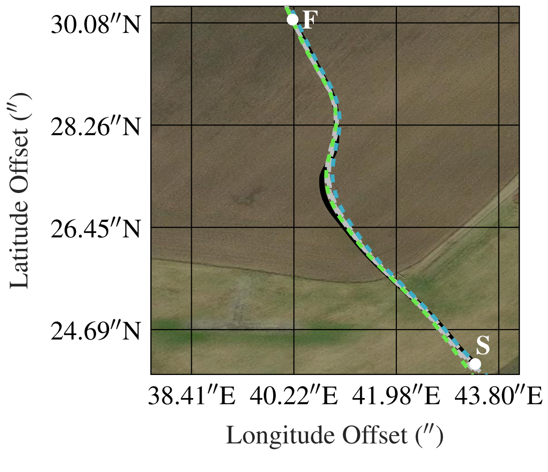

Fig. 12. Test flights ground tracks (- - -) with the most (- - -) and least (- - -) accurate flight along the flight path (━━) relative to the reference point at (N 50°58′, E 13°44′).

expressed relative to a reference point at (N 50°58′, E 13°44′). Two representative flights are examined in more detail, namely the flight which shows the smallest maximum lateral deviation and thus the highest tracking accuracy (flight A,), and the flight with the largest maximum lateral deviation from the trajectory (flight B). The ground tracks for flight A (- - -) and flight B (- - -) are depicted in Fig. 12. Both flights generally show an adequate tracking of the demanded trajectory.

To quantify the lateral tracking performance, the horizontal smallest deviation between the aircraft position and the trajectory is computed for each point in time. The results for flight A (—) and flight B (—) are presented in Fig. 13. The black dotted line marks the moment at which the aircraft first reaches the beginning of the trajectory, while the colored dashed lines (green and blue for flights A and B, respectively) indicate when the end of the trajectory is reached. The maximum lateral deviation, indicated with the orange line, occurs during flight B in the first turn and amounts to a distance of 4.12 m, showing satisfactory behavior. For the longitudinal performance the altitude tracking is analyzed. Since the desired trajectory has a constant altitude of 433 m MSL, the guidance demands flight-path angles to keep the UAV at this level. In Fig. 14 the altitude progression of the UAV along the trajectory is depicted for flight A (—) and flight B (—) together with the desired altitude (—). In both cases the deviation successfully remains within ±1 m, with the errors being bounded by the depicted orange lines. A summary of the maximum lateral deviation e_d^* and the maximum altitude deviation e_h^* for each flight is provided in Table 1, where flight 4 and flight 7 correspond to flight A and flight B, respectively. The analysis of the tracking results indicate that across the seven test sequences the guidance and control system provides adequate tracking of the trajectory.

Table 1. Max. trajectory deviations for each flight

Flight Nr.	1	2	3	4 (A)	5	6	7 (B)
e_d^* (m)	2.23	1.95	1.83	1.77	2.75	2.40	3.90
e_h^* (m)	0.30	0.25	0.29	0.47	0.27	0.34	0.98

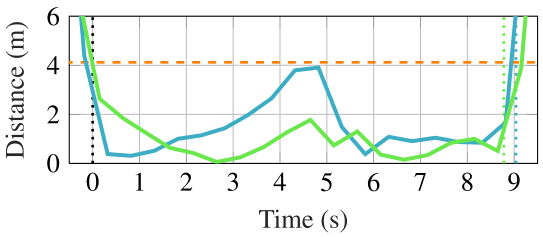

Fig. 13. Distance to the nominal trajectory for the most (—) and least (—) accurate flight.

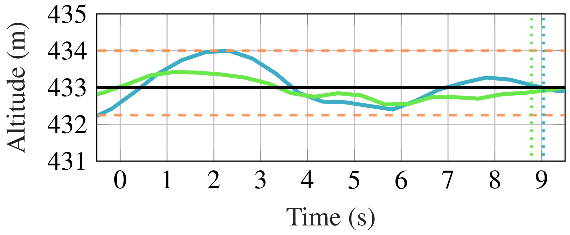

Fig. 14. Altitude compared to the reference altitude (—) during the most (—) and least (—) accurate flight.

6. CONCLUSION

An integrated guidance and control architecture for small fixed-wing unmanned aerial vehicles is presented. This co-design of guidance and control loops enables highly dynamic flight trajectories while respecting the constraints inherent to these small-scale aircraft. The proposed system architecture is applied to the Urban Condor X flight-test aircraft. Results from the flight test campaign confirm that the architecture enables precise tracking of highly dynamic trajectories, demonstrating its effectiveness and practical applicability.

REFERENCES

Berenguer Bertran, R., Biertümpfel, F., and Pfifer, H. (2025). Guidance and Control of an Unmanned Aerial Vehicle Along Energy Optimal Trajectories. In *AIAA Scitech Forum*. Orlando, FL, USA.

Bosio, C. and Mueller, M.W. (2025). Automated Layout and Control Co-Design of Robust Multi-UAV Transportation Systems. *IEEE Robotics and Automation Letters*, 10(4), 3956–3963.

Franke, A., Guist, M., Wisbacher, S., Ossmann, D., and Pfifer, H. (2026). Flight Test Based System Identification of an Unmanned Fixed-Wing Aircraft. In *CEAS EuroGNC*. Madrid, Spain.

Mabboux, J., Pommier-Budinger, V., Delbecq, S., and Bordeneuve-Guibe, J. (2024). Co-design of a multirotor UAV with robust control considering handling qualities and motor failure. *Aerospace Science and Technology*, 144, 108778.

Park, S., Deyst, J., and How, J. (2004). A New Nonlinear Guidance Logic for Trajectory Tracking. In *AIAA Guidance, Navigation, and Control Conference and Exhibit*. Providence, RI, USA.

Razar, N. (2008). Lateral Guidance & Control Design for an Unmanned Aerial Vehicle. In *17th IFAC World Congress*. Seoul, South Korea.

Rienecker, H., Hildebrand, V., and Pfifer, H. (2025). Energy Optimal Flight Path Planning for Unmanned Aerial Vehicles in Urban Environments Considering Trajectory Uncertainties. In *AIAA Scitech Forum*. Orlando, FL, USA.

Schmidt, D.K. (2012). *Modern Flight Dynamics*. Connect, Learn, Succeed. McGraw-Hill.

Sedlmair, N., Theis, J., and Thielecke, F. (2022). Flight Testing Automatic Landing Control for Unmanned Aircraft Including Curved Approaches. *Journal of Guidance, Control, and Dynamics*, 45(4), 726–739.

Skogestad, S. and Postlethwaite, I. (2005). *Multivariable Feedback Control: Analysis and Design*. John Wiley & Sons.

Theis, J., Ossmann, D., Thielecke, F., and Pfifer, H. (2018). Robust autopilot design for landing a large civil aircraft in crosswind. *Control Engineering Practice*, 76, 54–64.

Theis, J., Pfifer, H., and Seiler, P. (2020). Robust modal damping control for active flutter suppression. *Journal of Guidance, Control, and Dynamics*, 43(6), 1056–1068.

Wauters, J., Lefebvre, T., and Crevecoeur, G. (2023). Multi-Objective Co-Design for Mission-Specific Development of Unmanned Aerial Systems. In *IEEE/ASME Int. Conference on Advanced Intelligent Mechatronics*. Seattle, WA, USA.

Wisbacher, S., Ossmann, D., Schubert, S., Frey, J., and Pfifer, H. (2025). Wind Tunnel Based System Identification of a Small Unmanned Aircraft System. In *AIAA Scitech Forum*. Orlando, FL, USA.